

Dissipative structures in optomechanical cavities

Joaquín Ruiz-Rivas,¹ Carlos Navarrete-Benlloch,² Giuseppe Patera,³ Eugenio Roldán,¹ and Germán J. de Valcárcel¹

¹*Departament d'Òptica, Universitat de València, Dr. Moliner 50, 46100 Burjassot, Spain*

²*Max-Planck-Institut für Quantenoptik, Hans-Kopfermann-Strasse 1, D-85748 Garching, Germany*

³*Laboratoire PhLAM, Université Lille 1, 59655 Villeneuve d'Ascq Cedex, France*

(Received 7 December 2012; revised manuscript received 15 February 2016; published 28 March 2016)

Motivated by the increasing interest in the properties of multimode optomechanical devices, here we study a system in which a driven longitudinal mode of a large-area optical cavity is dispersively coupled to a deformable mechanical element. Two different models naturally appear in such scenario, for which we predict the formation of periodic patterns, localized structures (cavity solitons), and domain walls, among other complex nonlinear phenomena. Further, we propose a realistic design based on intracavity membranes where our models can be studied experimentally. Apart from its relevance to the field of nonlinear optics, the results put forward here are a necessary step towards understanding the quantum properties of optomechanical systems in the multimode regime of both the optical and the mechanical degrees of freedom.

DOI: [10.1103/PhysRevA.93.033850](https://doi.org/10.1103/PhysRevA.93.033850)

I. INTRODUCTION

Since the 1980s, the advent and rapid growing of quantum information have boosted the research on quantum technologies that try to develop microdevices allowing for robust implementations of controllable quantum interactions for long coherence times. By today the state of the art permits the fabrication of devices functioning in such a strong coupling regime with unprecedented control and accuracy in a flourishing field. These new quantum devices are very diverse, including cavity-QED [1], optical lattices [2], trapped ions [3], superconducting circuits [4], quantum dots [5], atomic ensembles [6], etc.

In typical optomechanical cavities [7] the interaction occurs between a light mode and a mechanical oscillator via radiation pressure. This type of system has long been known in classical optics [8] and to some extent resembles a nonlinear Kerr cavity [9] because the cavity length (and consequently the cavity resonance) depends on the intracavity field intensity. At present, the focus is on their capability to show quantum coherent phenomena such as cooling and amplification [10] and strong (linear) coupling effects like optomechanically induced transparency [11] or to prepare squeezed states of light dissipatively [12–15]. Attention has also been recently paid to the nonlinear dynamics of optomechanical arrays [16], cavities in which radiation pressure competes with the photothermal effect [17], planar dual-nanoweb waveguides subject to radiation pressure [18], and optomechanical cavities containing atomic ensembles [19].

Except for some of these recent works, most studies deal so far with a small number of modes in either the optical or the mechanical degrees of freedom, while the nonlinear interplay between many optical and mechanical modes entails the existence of correlations among them that can provide optomechanical systems with new capabilities. At the quantum level, these correlations may lead to multipartite entanglement [20–22]; at the classical level, they help for the spontaneous appearance of dissipative structures that are long-range ordered configurations, including periodic, quasiperiodic, and aperiodic patterns, as well as localized structures, which may also exhibit nontrivial temporal behavior [23].

The interplay between the quantum and the classical perspectives in multimode systems has received theoretical attention mainly in the context of optical parametric oscillators for which some exciting phenomena were predicted [24]. No such studies exist concerning optomechanical systems, and here we make a step towards this goal by proposing a multimode optomechanical cavity configuration in which dissipative structures are predicted to appear. We keep our study at the classical level by showing that such patterns can appear and how they appear, leaving the study of their quantum properties for a future publication. As we show below, periodic patterns, localized structures (cavity solitons), and domain walls are predicted to occur in a wide region of the two models that naturally follow from the proposed configuration.

II. MODEL

We consider an optical cavity with large-area mirrors containing a dispersive, transparent membrane, which can be deformed locally, but which is also allowed to oscillate as a whole along the cavity axis (Fig. 1). Energy is fed into the cavity by injecting a coherent laser field E_{inj} of angular frequency ω_L , close to a cavity longitudinal mode of frequency ω_c , through a (partially transmitting) mirror,

$$E_{\text{inj}}(z, \mathbf{r}, t) = i\mathcal{V}A_{\text{inj}}(z, \mathbf{r}, t)e^{i(k_L z - \omega_L t)} + \text{c.c.}, \quad (1)$$

where $\mathbf{r} = (x, y)$ denotes the position on the plane transverse to the cavity axis (z axis), $k_L = \omega_L/c$, and \mathcal{V} is a constant having the dimensions of voltage, which we choose as $\mathcal{V} = \sqrt{\hbar\omega_c/4\epsilon_0 L}$ in order to make contact with quantum optics (see Appendix A and [24]). The intracavity field $E(z, \mathbf{r}, t)$ can be written generically as

$$E(z, \mathbf{r}, t) = i\mathcal{V}(A_+ e^{ik_L z} + A_- e^{-ik_L z})e^{-i\omega_L t} + \text{c.c.}, \quad (2)$$

which is the superposition of two waves with slowly varying complex amplitudes $A_{\pm}(z, \mathbf{r}, t)$, propagating along the positive (A_+) and negative (A_-) z direction. We first derive an evolution equation for the amplitude $A_+(z = L, \mathbf{r}, t)$ at the end mirror's surface, which we denote by $A(\mathbf{r}, t)$. The procedure, which we detail in Appendix A, consists of propagating the field along a full cavity round trip in the paraxial approximation

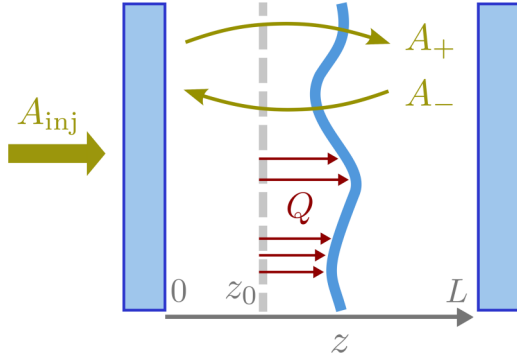


FIG. 1. Illustration of the system.

and treating the membrane as a thin (subwavelength, as commercial membranes are typically 50 nm thick) deformable beam splitter. The local displacement of the membrane perpendicular to its rest position (at $z = z_0$) is measured by the field $Q(\mathbf{r}, t)$; hence, $Q = 0$ in the absence of illumination. Assuming that the field changes very little after one round trip (which requires highly reflective mirrors, a small reflectance ϱ^2 of the membrane, small detuning, and small diffraction), the field equation can be written as

$$\gamma_c^{-1} \partial_t A(\mathbf{r}, t) = \mathcal{E}(\mathbf{r}, t) + (-1 + i\Delta + il_c^2 \nabla_{\perp}^2) A - i \frac{4\varrho}{T} \cos[2k_L(z_0 + Q)] A, \quad (3)$$

where $\gamma_c \equiv cT/4L$ is the cavity damping rate ($T \equiv T_1 + T_2$ is the sum of the mirrors' transmittances), $\mathcal{E}(\mathbf{r}, t) \equiv (2\sqrt{T_1}/T) A_{inj}(0, \mathbf{r}, t)$ is a scaled version of the injection field amplitude, and $\Delta \equiv (\omega_L - \omega_c)/\gamma_c$ is the dimensionless detuning parameter. Finally, the term $il_c^2 \nabla_{\perp}^2 A$ represents diffraction, with $\nabla_{\perp}^2 \equiv (\partial_x^2 + \partial_y^2)$ the transverse Laplacian operator and $l_c^2 \equiv 2L_{diff}/k_L T$ the transverse diffraction length (squared). The quantity L_{diff} represents the effective cavity length (from the viewpoint of diffraction), which can be made different from L by using quasi-self-imaging resonators [25], which we consider in our proposal. In such resonators, extra elements such as lenses or other mirrors are used to image both end mirrors very close to each other, the separation between their images being L_{diff} . These types of resonators are commonly used in experiments of optical pattern formation [26,27], nonlinear imaging [28], spatially multimode squeezing [29], and more recently in optomechanics [30]. They offer a flexible way to control the intracavity diffraction because L_{diff} can be tuned at will, in both magnitude and sign (in the following we consider $L_{diff} \geq 0$).

The equation for the light field must be complemented with an equation for the displacement field $Q(\mathbf{r}, t)$. In the absence of forcing Q obeys a damped wave equation $\partial_t^2 Q + \gamma_m \partial_t Q + \mathbb{L}Q = 0$, where \mathbb{L} is a suitable differential operator whose form depends on the specific implementation, and γ_m is a damping constant (damping is assumed homogeneous for simplicity). As explained in Appendix B, coupling of the membrane to the light field modifies the above wave equation to

$$\partial_t^2 Q + \gamma_m \partial_t Q + \mathbb{L}Q = \frac{4\varrho \hbar k_L}{\sigma t_c} \sin[2k_L(z_0 + Q)] |A|^2, \quad (4)$$

where σ is the membrane's surface mass density, and $t_c \equiv 2L/c$ is the cavity round-trip time.

For the sake of simplicity and analyticity, we choose $\mathbb{L} = \Omega_m^2 - v_m^2 \nabla_{\perp}^2$, which models a membrane (characterized by its sound speed v_m) that can oscillate as a whole at frequency Ω_m . This choice ensures that the model will possess spatially homogeneous solutions (invariant under translations across the transverse plane), which can become unstable in favor of patterns that break such symmetry, as usual in spontaneous pattern-forming scenarios [31]. As we show below through numerical simulations, the existence of such sufficiently homogeneous solutions turns out to be essential for pattern formation, and later we propose a specific experimental implementation leading to this particular choice of \mathbb{L} .

Equations (3) and (4) constitute the basic model for our optomechanical setup. Upon ignoring spatial effects therein ($\nabla_{\perp}^2 \rightarrow 0$) the model coincides with previous single-mode models [32,33] in the limit of small reflectance ϱ^2 , which we have assumed. Note that in these setups the optomechanical coupling arises from the boundary conditions that the membrane imposes on the electromagnetic field, which depend on its position. It is well known that this general model depends strongly on the location z_0 of the membrane in the absence of illumination. In this work we consider the two typical special situations [32,33] in which either (i) the membrane is located at a node of the driven mode's standing wave ($z_0/\lambda_L = 0, 1/2, 1, \dots$), (ii) or it is half-way between a node and an antinode ($z_0/\lambda_L = 1/8, 3/8, 5/8, \dots$). We refer to the corresponding models as the *quadratic* and *linear* models, respectively, because this is the approximate dependence that the light's frequency shift $4\varrho \cos[2k_L(z_0 + Q)]/T$ has on the mechanical field on each case; see last term in Eq. (3). These special models are obtained from Eqs. (3) and (4) as usual, by Taylor expanding the sin and cos functions in terms of the membrane's displacement around $Q = 0$ to the first nontrivial order in Q (see Appendix C). The two resulting models can be written in a compact and clean form by introducing an index μ , which equals 1 or 2 for the linear or quadratic models, respectively, as well as normalized variables and parameters. Defining the dimensionless time $\tau \equiv \gamma_c t$, spatial coordinates $\bar{\mathbf{r}} \equiv \mathbf{r}/l_c$, plus parameters $\gamma \equiv \gamma_m/\gamma_c$ and $\Omega \equiv \Omega_m/\gamma_c$, we get (Appendix C)

$$\partial_{\tau} F = E + [-1 + i(\Delta_{\mu} + \nabla^2 + Z^{\mu})] F, \quad (5a)$$

$$\partial_{\tau}^2 Z + \gamma \partial_{\tau} Z + \Omega^2(1 - \rho^2 \nabla^2) Z = \Omega^2 Z^{\mu-1} |F|^2, \quad (5b)$$

where F , Z , and E are normalized dimensionless versions of the optical field A , the mechanical field Q , and the pump \mathcal{E} , respectively (see Appendix C), $\nabla^2 \equiv (\partial_{\bar{x}}^2 + \partial_{\bar{y}}^2)$, $\Delta_{\mu} \equiv \Delta - 4(\mu - 1)\varrho/T$, and we have defined the “effective rigidity” parameter

$$\rho \equiv v_m/\Omega_m l_c, \quad (6)$$

so that the larger ρ the more rigidly the membrane behaves. Alternatively, ρ is a measure of how local the response of the membrane is to a stress: When $\rho \rightarrow 0$, the response is local, while for $\rho \rightarrow \infty$ it is completely integrated; that is, only the homogeneous mode is excited.

Let us remark that we have also considered the situation in which the end mirror is the deformable mechanical element, optomechanical coupling arising from the radiation pressure force [7] in such case. The resulting normalized model coincides with the linear model introduced above in Eq. (5), with $\mu = 1$. Also, note that we have not included the case of the membrane being in an antinode ($z_0/\lambda_L = 1/4, 3/4, 5/4, \dots$), which results in a model like the one above with $\mu = 2$ but with an extra negative sign in front of the terms Z^μ and $Z^{\mu-1}$ (see Appendix C), because we have not found any pattern-forming instabilities in such configuration.

III. HOMOGENEOUS SOLUTIONS, THEIR STABILITY, AND PATTERN FORMATION

When the injected field is a plane wave propagating along the cavity axis, the amplitude E is a constant, which we take as real and positive without loss of generality (this sets a reference phase). In such a case Eqs. (5) admit spatially homogeneous solutions which coincide with the well-known ones of the single-mode models [7], which are retrieved from Eqs. (5) with $\nabla^2 \rightarrow 0$.

In the linear model (LM, $\mu = 1$), the stationary homogeneous solutions verify $\bar{Z}_{\text{LM}} = |\bar{F}_{\text{LM}}|^2$ (overbars denote steady homogenous solutions), with

$$E^2 = [1 + (\Delta + \bar{Z}_{\text{LM}})^2] \bar{Z}_{\text{LM}}. \quad (7)$$

This is the usual state equation of the single-mode optomechanical cavity (or of a Kerr cavity), which shows a bistable response whenever $\Delta < -\sqrt{3}$; see Figs. 2(a) and 2(b).

Differently, in the quadratic model (QM, $\mu = 2$), there are two homogeneous steady states that bifurcate one into the other: the trivial state, for which $\bar{Z}_{\text{QM}} = 0$ and $\bar{F}_{\text{QM}} = E/(1 - i\Delta)$, and the nontrivial one,

$$\bar{Z}_{\text{QM}} = \pm \sqrt{\sqrt{E^2 - 1} - \Delta}, \quad |\bar{F}_{\text{LM}}|^2 = 1, \quad (8)$$

which exists only for $E^2 > (1 + \Delta^2)$. Note that for $\Delta < 0$ there is a pump region where the trivial and nontrivial solutions coexist; see Figs. 2(c) and 2(d).

These spatially homogeneous steady states can suffer different instabilities leading to the appearance of new solutions, such as self-pulsing or spatially modulated solutions (through Hopf or pattern-forming bifurcations, respectively). The latter break spontaneously the translational invariance of the model and are the subject of the present study. Standard linear stability analysis techniques allow us to derive the location of these bifurcations in the parameter space (see Appendix D). We have performed an exhaustive analysis which has revealed a rich phenomenology that goes beyond the scope of the present work, whose goal is to evidence the possibility of pattern formation in optomechanical cavities. We will present the full picture elsewhere, but here we want to comment on some general trends and focus on representative examples.

Both linear and quadratic models show a static pattern-forming instability, as well as a Hopf instability. The latter leads either to a pulsing homogeneous state (homogeneous Hopf bifurcation) or to a pulsing structure (pattern forming Hopf bifurcation), depending on the system parameters. Together with the homogeneous stationary solutions \bar{Z} , in

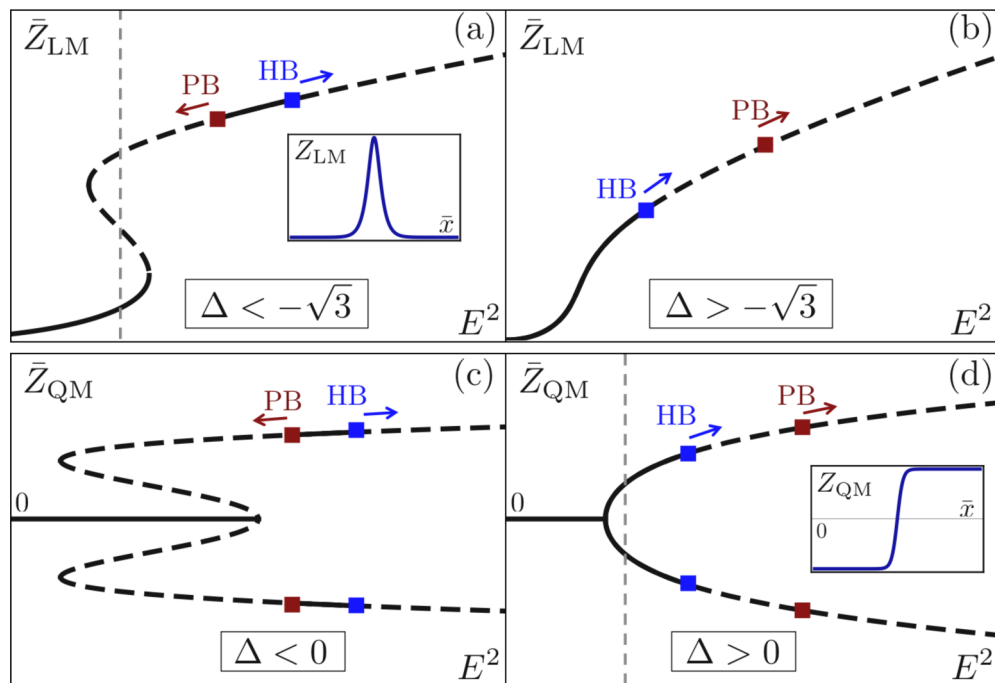


FIG. 2. (a)–(d) Illustration of the generic steady-states and instabilities of the linear (LM) and quadratic (QM) models introduced in the text. We plot the mechanical displacement \bar{Z} of the homogeneous steady-state solution as a function of the injection E^2 , with the stable (unstable) regions denoted by solid (dashed) lines. We mark the pitchfork bifurcation leading to pattern formation (red squares), as well as the Hopf instability (blue squares) leading to oscillatory solutions, the arrows indicating the portion of the curve which they make unstable. The insets in (a) and (d) show the type of patterns expected for injections marked by the thin gray line, corresponding to solitons in the linear model and domain walls in the quadratic one.

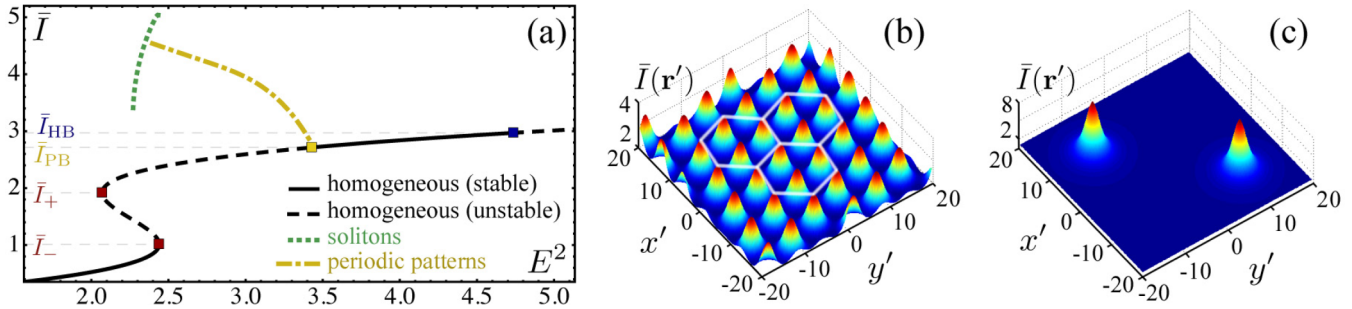


FIG. 3. Numerical simulation of the linear model equations. In (a) we show the bifurcation diagram for $\Delta = -2.2$, $\gamma = 0.1$, $\Omega = 10$, and $\rho = 1.13$, parameters which we use in this example. The intensity \bar{I} of the homogeneous steady-state solution is plotted as a function of the injection E^2 , denoting by solid (dashed) lines the stable (unstable) regions. We mark with a yellow square the static pattern-forming instability at $\bar{I} = \bar{I}_{PB}$, as well as the rest of instabilities mentioned in the text. Patterns are expected to appear for injections within the unstable domain of the upper branch occurring for $\bar{I}_+ < \bar{I} < \bar{I}_{PB}$. We have found two types of patterns: periodic (hexagonal in 2D) patterns (b), whose maximum (as obtained from a 1D simulation) is represented as a yellow dash-dotted line in their domain of existence, and localized structures (c), represented as a green dotted line, which can be “written” and “erased” individually at any desired position in the transverse plane by injecting an pulse of Gaussian transverse profile with the proper width and centered at the corresponding point. At $\bar{I} = \bar{I}_{HB}$ the steady state undergoes a Hopf bifurcation leading to time-dependent long-time term solutions (limit cycles) not shown in the figure.

Fig. 2 we have marked the typical location of these instabilities, as well as the regions of \bar{Z} that become unstable. In very general terms, we can say that the existence of pattern-forming instabilities requires a rigidity ρ below some maximum value ρ_c ; for the linear model ($\mu = 1$) we have $\rho_c = 1$ for $\Delta \geq -\sqrt{3}$ and $\rho_c > 1$ for $\Delta < -\sqrt{3}$, while for the quadratic one ($\mu = 2$) we have $\rho_c = 1$ for $\Delta \geq 1/2$ and $\rho_c = -2\Delta$ for $\Delta < -1/2$. As for the Hopf instability, we can also say that the smaller γ or the larger Ω are, the closer it is to the limit of existence of the nonzero solutions, in particular tending to invade the whole domain of existence of the nontrivial solution for small γ in the quadratic model.

In order to study the type of patterns appearing in the unstable regions, we have performed a numerical analysis of the model equations in both one (1D) and two (2D) transverse dimensions using a split-step method with periodic boundary conditions (see Appendix E). In Fig. 3 we show examples of such structures as obtained from the linear model, Eqs. (5) with $\mu = 1$, as well as their location in the bifurcation diagram.

Our analysis has revealed periodic patterns (hexagonal in 2D) and localized structures, as well as more complex spatiotemporal phenomena. Remarkably, stable localized structures appear in the regions where there is coexistence between the stable lower branch and the unstable upper branch solutions in the linear model [see the inset of Fig. 2(a)] or between the stable trivial and the unstable nontrivial solutions in the quadratic one. We have checked that these localized structures can be written, erased, and moved individually, so that they behave as true cavity solitons [34]. An important difference between the two models is that the quadratic one has intrinsic phase bistability, since $Z(\bar{\mathbf{r}}, \tau) \rightarrow -Z(\bar{\mathbf{r}}, \tau)$ leaves the equations invariant, which leads to the existence of domain walls that appear between two adjacent regions occupied by solutions differing only in their sign [see the inset of Fig. 2(d)].

IV. PHYSICAL IMPLEMENTATION

State-of-the-art optomechanical setups allow for the use of silicon nitride membranes both as intracavity elements

dispersively coupled to the light contained in the resonator [32,33,35–40] and directly as end mirrors, hence sensitive to radiation pressure [41–43]. In all these experiments the membrane is held by a fixed frame, so that the membrane cannot be displaced as a whole in the axial direction. Such systems are then described by our 2D model equations (3) and (4), with $\mathbb{L} = -v_m^2 \nabla_{\perp}^2$ (i.e., with $\Omega_m = 0$ because there is no homogeneous mechanical mode) and Dirichlet boundary conditions $Q|_{\text{boundary}} = 0$.

In order to deal with dimensionless equations, normalizations different from the ones used so far must be set, because F , E , and Q diverge in the limit $\Omega_m = 0$, as can be appreciated from Eqs. (C5) and (C10). In order to avoid this problem, we still use normalizations (C5) and (C10), but with Ω_m being replaced by γ_c , obtaining

$$\partial_{\tau} F = E + [-1 + i(\Delta_{\mu} + \nabla^2 + Z^{\mu})]F, \quad (9a)$$

$$\partial_{\tau}^2 Z + \gamma \partial_{\tau} Z - v^2 \nabla^2 Z = Z^{\mu-1} |F|^2, \quad (9b)$$

where we have introduced the normalized sound speed,

$$v = v_m / \gamma_c l_c. \quad (10)$$

Note that Eqs. (9) are retrieved formally from Eqs. (5) by setting $\Omega = 1$ and removing the “1” inside the term $\Omega^2(1 - \rho^2 \nabla^2)Z$ in Eq. (5b). Equation (9) contain two “structural parameters,” γ and v , plus two tunable parameters, E and Δ . Apart from these, the physical solutions that they lead to depend on the integration region (shape and size).

We have performed extensive numerical simulations of Eqs. (9) on square membranes with $Z|_{\text{boundary}} = 0$, obtaining no dissipative structures (periodic patterns or cavity solitons); of course, deformations of the membrane appear which, in turn, modify the light field profile, leading, in general, to irregular distributions, but these structures are strongly determined by the boundary conditions and then are not spontaneous patterns. We relate this negative result to the absence of a spatially homogeneous solution of Eqs. (9), in agreement with the intuition we provided when first introducing the differential

operator as $\mathbb{L} = \Omega_m^2 - v_m^2 \nabla_{\perp}^2$. Hence, it might seem that the patterns and solitons we have presented so far are merely mathematical, as model (5) seems to have no immediate physical implementation. However, we show in what follows that quasi-1D geometries indeed allow for the implementation of such model.

Let us assume that the membrane is not a square but has a rectangular shape with unequal lengths L_x and L_y along the x and y directions, respectively. For the sake of argumentation, consider a frame that only clamps two opposite sides of the membrane (say the upper and lower sides, located at $y = \pm L_y/2$), leaving unclamped the right and left sides, located at $x = \pm L_x/2$. It is then clear that spatially homogeneous states exist along the horizontal direction (x) of the membrane, while the membrane is flexed along the vertical (y) direction. Under these conditions we envisage that 1D patterns should be observable along the x direction. In order to make this idea more formal, albeit not necessarily rigorous, and gain insight into the problem, let us assume an idealized situation in which only the fundamental flexural mode along the y direction of the membrane is excited, so that the membrane's field Z can be written as $Z(\bar{\mathbf{r}}, t) = \cos(\pi \bar{y}/\bar{L}_y) Z_{1D}(\bar{x}, t)$, with $\bar{L}_{x,y} = L_{x,y}/l_c$ and $\bar{y} \in [-\bar{L}_y/2, +\bar{L}_y/2]$, leading to

$$-v^2 \nabla^2 Z \equiv \Omega_{\text{eff}}^2 (1 - \rho_{\text{eff}}^2 \partial_{\bar{x}}^2) Z, \quad (11)$$

with

$$\Omega_{\text{eff}} = \pi v / \bar{L}_y = \pi v_m / \gamma_c L_y, \quad (12a)$$

$$\rho_{\text{eff}} = \bar{L}_y / \pi = L_y / \pi l_c. \quad (12b)$$

This way, Eq. (9b) becomes

$$\partial_{\bar{t}}^2 Z + \gamma \partial_{\bar{t}} Z + \Omega_{\text{eff}}^2 (1 - \rho_{\text{eff}}^2 \partial_{\bar{x}}^2) Z = Z^{\mu-1} |F|^2, \quad (13)$$

which is similar to a 1D version of Eq. (5b) with effective parameters Ω_{eff} and ρ_{eff} . If the ends of the membrane along the x direction are free, as we have assumed, Eq. (13) formally evidences the existence of a spatially homogeneous mode along the x direction. Moreover, we can use the knowledge gained when studying model (5) to predict for which parameters the dissipative structures will appear in this quasi-1D geometry. There are basically two requirements for the appearance of such structures: (i) the effective rigidity ρ_{eff} has to be smaller than a certain value ρ_c , which in the smallest case was found to be 1, i.e., $L_y \lesssim \pi l_c \rho_c$; (ii) the x direction must have a length $L_x \gg l_c$ in order to have sufficient room for spatial structures. The rest of the parameters do not impose relevant constraints, as we have shown above.

Let us discuss now whether these conditions can be satisfied with current technology. Starting from condition (ii), and using $L_x = 1$ mm (typical in commercial silicon nitride membranes [32,33,35–40]), let us take $l_c = 50$ μm , so that $L_x = 20l_c$. Then, in the most restrictive case ($\rho_c = 1$) condition (i) reads $L_y \lesssim 50\pi$ μm , so we can then take $L_y = 150$ μm (i.e., the membrane should be striplike). The latter is just a matter of proper design of the frame, while the chosen value for l_c is obtained by fixing the effective diffractive length of the cavity L_{diff} : As $l_c = \sqrt{\lambda_L L_{\text{diff}} \mathcal{F}} / 2\pi$, with $\mathcal{F} = 2\pi/T$ the cavity finesse, using $\lambda_L = 1064$ nm, and $\mathcal{F} = 5 \times 10^4$ [40] or 1.5×10^4 [32] we get, respectively, $L_{\text{diff}} = 1.855$ or 6.184 μm .

The tolerance in the value of L_{diff} is given, roughly, by the condition $l_c = L_y / \pi = 48$ μm , which is reached when $L_{\text{diff}} = 1.710$ μm for [40] or 5.700 μm for [32]; i.e., in this case L_{diff} should be experimentally set with a precision better than 145 nm [40] or 484 nm [32], safely larger than the typical 1-nm precision reached by available motorized stages [32,40]. Hence, we see that, in principle, the proposal seems implementable with state-of-the-art technology.

Regarding the normalized speed v that can be reached in experiments, we first need to know the values of v_m and γ_c ; see (10). The sound speed in the membrane can be deduced from previous experiments as follows: Taking the fundamental mode frequency of a 1-mm-side square membrane as $\Omega_{1,1}/2\pi = 134$ kHz [40] or 356 kHz [32] and taking into account that $\Omega_{1,1} = \sqrt{2\pi} v_m / (1 \text{ mm})$, we get $v_m \approx 200$ or 500 m/s, respectively, the difference probably being due to differences in the samples. As for the optical decay rates, we have $\gamma_c = 85$ kHz in [40] and 450 kHz in [32]. Using $l_c = 50$ μm and combining the different parameters of Refs. [32,40], we find normalized speeds in the range $v \approx 10$ – 100 . Note that this implies $\Omega_{\text{eff}} \approx 9$ – 100 ; see (12a). Moreover, by using larger (but still commercial) membranes with $L_x = 1.5$ mm, we can take $l_c = 75$ μm and $L_y = 225$ μm , leading to $\rho_{\text{eff}} \lesssim 1$ and $\Omega_{\text{eff}} \approx 6$. This means that there is a certain flexibility in designing the effective 1D model. Summarizing, we envisage conditions under which $\rho_{\text{eff}} \lesssim 1$ and $\Omega_{\text{eff}} \approx 6$ – 100 , in which we have found stable patterns in the (ideal) model with the homogeneous mode of Eqs. (5). Let us finally remark that, in order to keep the Hopf bifurcation as far away as possible, so that the generated patterns are static, it is desirable to work with membrane frequencies $\Omega_{1,1}$ as small as possible, and cavity decay rates γ_c as large as possible, leading to small effective frequencies Ω_{eff} .

All the above reasoning rests on the assumption that only the fundamental mode of the membrane along the (short) y direction is excited and that the membrane has free ends along the (long) x direction. We have performed extensive numerical simulations of Eqs. (9), which confirm this simple picture and, moreover, have allowed us to prove that even if the membrane is clamped along the x direction (as usual in framed commercial ones), a sufficiently homogeneous state still exists along that direction which allows for the emergence of dissipative structures. In Fig. 4 we present results for both the linear and the quadratic models, in particular showing a cavity soliton from the linear model and a domain wall from the quadratic one. We provide the particular parameters used in the simulations below, but we want to remark here that they are not of real relevance since the structures are robust and easily found within the region of the parameter space where they are expected to appear according to the effective 1D model.

The patterns presented in Fig. 4 have been found by solving Eqs. (9) supplemented by Dirichlet boundary conditions at the rectangular frame of the membrane; that is, $Z(\pm \bar{L}_x/2, \bar{y}) = 0 = Z(\bar{x}, \pm \bar{L}_y/2)$, which we directly impose in the split-step method. Moreover, we have considered a quasiplane injection of finite width given by the super-Gaussian profile $E(\bar{\mathbf{r}}) = E_0 \exp\{-\frac{1}{2}[(\bar{x}/\sigma_x)^{20} + (\bar{y}/\sigma_y)^{20}]\}$.

In Fig. 4(a) we show a soliton obtained from the linear model ($\mu = 1$), expected to appear wherever bistability is

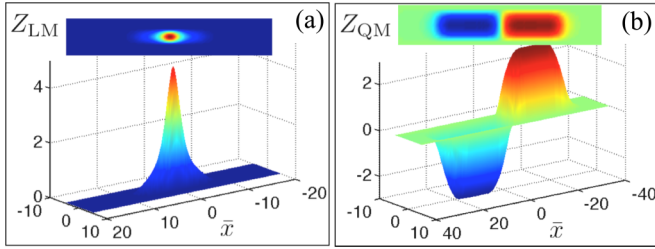


FIG. 4. Localized structures found by numerically solving the equations modeling a realistic implementation based on framed membranes, expected to lead to an effective 1D model with homogeneous mode and patterns occurring along the x axis, as long as only one or few modes of the membrane are excited in the y direction. In (a) we show that a soliton is appearing in the region marked with a vertical dashed line in Fig. 2(a), while in (b) we show a domain wall appearing in the region marked in Fig. 2(d). The specific parameters of the simulation in (a) are $\nu = 1$, $\gamma = 0.1$, and $\Delta = -2.2$, plus widths $\bar{L}_y = 3.125$ and $\bar{L}_x = 40$ for the membrane, and parameters $\sigma_x = 7$, $\sigma_y = 3$, and $E_0 = 1.45$ for the super-Gaussian injection. As for (b), we have chosen $\nu = \sqrt{0.1}$, $\gamma = 0.1$, $\Delta = 5$, $\bar{L}_y = 6.25$, $\bar{L}_x = 80$, $\sigma_x = 7.5$, $\sigma_y = 3$, and $E_0 = 6.8$.

present and the upper branch is unstable because of the static pattern-forming bifurcation; see Fig. 2(a). In order to be in this region, we have chosen model parameters (see the inset of Fig. 4 for specific values) leading to the effective 1D parameters $\rho_{\text{eff}} = 3.125/\pi \approx 0.995$ and $\Omega_{\text{eff}} \approx 10.05$ according to Eqs. (12a). On the other hand, in Fig. 4(b) we show a domain wall expected to appear in the quadratic model ($\mu = 2$) when the nontrivial homogeneous stationary solutions with opposite signs coexist; see Fig. 2(d). In this case we have chosen model parameters leading to effective 1D ones $\rho_{\text{eff}} = 6.25/\pi \approx 2$ and $\Omega_{\text{eff}} \approx 0.16$. Let us remark that we have not chosen a larger value of Ω because, otherwise, the Hopf bifurcation tends to the point where the trivial and nontrivial solutions connect, making it impossible to find stationary solutions above that point (although, interestingly, it is possible to find dynamic ones, such as pulsing domain walls). These simulations prove the feasibility of testing our predictions with current optomechanical technology.

V. CONCLUSIONS

We have proposed an optomechanical cavity system in which spontaneous pattern formation can be observed. In our proposal, the mechanical degrees of freedom come from a membrane which can be locally deformed by its interaction with light. Two different models appear in this scenario (linear and quadratic interactions), for which we have been able to locate their pattern forming instabilities. An important conclusion of our numerical investigations is that the existence of such structures requires the presence of a sufficiently homogeneous mechanical mode, and we have proposed realistic implementations of the 1D models based on currently available membranes, proving how patterns (solitons and domain walls) indeed appear in such systems. Future venues will include the study of the quantum spatial correlations present on (and between) the optical and mechanical fields, which may lead to noncritical squeezing and multipartite

entanglement, similarly to what has been found in optical parametric oscillators [24,44].

ACKNOWLEDGMENTS

We acknowledge fruitful discussions with Chiara Molinelli. This work has been supported by the Spanish Government and the European Union FEDER through Projects No. FIS2011-26960 and No. FIS2014-60715-P. J.R.-R. is a grant holder of the FPU program of the Ministerio de Educación, Cultura y Deporte (Spain). C.N.-B. acknowledges the financial support of the Future and Emerging Technologies (FET) programme within the Seventh Framework Programme for Research of the European Commission, under the FET-Open Grant Agreement MALICIA, No. FP7-ICT-265522, and of the Alexander von Humboldt Foundation through its Fellowship for Postdoctoral Researchers.

APPENDIX A: DERIVATION OF THE LIGHT FIELD EQUATION

In this section we offer a detailed derivation of Eq. (3) in the main text, which describes the evolution of the optical field at the plane of the end mirror.

1. Basic derivation

Let us first consider a simple cavity geometry consisting of two mirrors facing each other; see Fig. 5. We denote by r_1 (r_2) the reflection coefficients of the left (right) cavity mirrors, $1 - |r_j|^2 = T_j$ being the corresponding transmittances, which are assumed very close to zero: good cavity limit. The left (right) mirror is located at $z = 0$ (L), and we assume for definiteness that light is injected through the left mirror.

In the absence of illumination the membrane has an equilibrium position at $z = z_0$, while in the presence of optical fields any point \mathbf{r} of the membrane will be displaced along the cavity axis by $Q(\mathbf{r}, t)$ from equilibrium, which defines the mechanical field introduced in the main text. We treat this deformable membrane as a thin, lossless symmetric beam splitter, with (complex) transmission and reflection coefficients denoted by τ_{\pm} and ϱ_{\pm} , where the subscript refers to the side of the membrane from which the beam emerges after transmission or reflection (+ for right and - for left). As in any lossless beam splitter [45], the phases of these coefficients

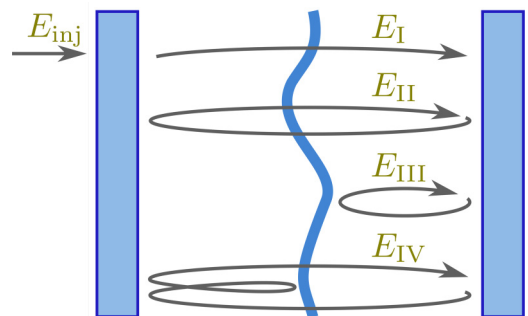


FIG. 5. Sketch of the paths traveled by the main waves superposing at the right cavity mirror at a given instant.

satisfy

$$\arg(\varrho_+) + \arg(\varrho_-) - \arg(\tau_+) - \arg(\tau_-) = \pi, \quad (\text{A1})$$

while further for a symmetric one,

$$|\tau_{\pm}| = \tau, \quad |\varrho_{\pm}| = \varrho, \quad (\text{A2})$$

with the relation $\tau^2 + \varrho^2 = 1$.

At any point in space and time, we write the optical field as $E(z, \mathbf{r}, t) = E_+(z, \mathbf{r}, t) + E_-(z, \mathbf{r}, t)$, which is a sum of two waves traveling to the right (+) and to the left (-). We choose arbitrarily to derive the evolution equation for the field $E_+(L, \mathbf{r}, t)$ impinging the right cavity mirror. Such an equation is derived by following the usual approach of propagating the field along the resonator (see, e.g., [26]), assuming that any modification of the field along a cavity round trip (due to diffraction and to transmission and reflection on the membrane or on the cavity mirrors) is small. This means that we are considering (i) short enough propagation distances (either geometrically small, or optically small, as in quasi-self-imaging resonators [25]) and (ii) membranes with very small reflectivities, $\varrho \ll 1$. The presence of the intracavity membrane makes the derivation a bit complicated because, at any instant, $E_+(L, \mathbf{r}, t)$ is the superposition of infinitely many contributions, corresponding to waves that have traveled in the cavity through paths with different combinations of transmissions and reflections in the membrane and the mirrors and meet at the right mirror. However, as the membrane reflectivities ϱ_{\pm} are assumed small, $E_+(L, \mathbf{r}, t)$ can be approximated at any instant as the sum of just four partial waves, as sketched in Fig. 5: (I) the injected field transmitted through the input mirror and the membrane (call it E_i), (II) the field that, after reflection on the right cavity mirror, has performed a full cavity round trip just by transmitting through the membrane (call it E_{II}); (III) the field that, after reflection on the right cavity mirror, reflects back from the right face of the membrane (call it E_{III}); and (IV) the field that, after transmission through the membrane and reflection on the left cavity mirror, has reflected from the left side of the membrane, reflected again from the left mirror, and finally transmitted through the membrane (call it E_{IV}). Any other partial wave has an amplitude on the order of ϱ^2 or smaller, which we neglect. Hence, we write

$$E_+(L, \mathbf{r}, t) = E_i(\mathbf{r}, t) + E_{II}(\mathbf{r}, t) + E_{III}(\mathbf{r}, t) + E_{IV}(\mathbf{r}, t), \quad (\text{A3})$$

where the four partial waves can be written as

$$E_i(\mathbf{r}, t) = K_i \mathcal{U}_L E_{\text{inj}}(0, \mathbf{r}, t - t_c/2), \quad (\text{A4a})$$

$$E_{II}(\mathbf{r}, t) = K_{II} \mathcal{U}_{2L} E_+(L, \mathbf{r}, t - t_c), \quad (\text{A4b})$$

$$E_{III}(\mathbf{r}, t) = K_{III} \mathcal{U}_{L_2} e^{-2ik_L Q(\mathbf{r}, t - t_2)} \times \mathcal{U}_{L_2} E_+(L, \mathbf{r}, t - 2t_2), \quad (\text{A4c})$$

$$E_{IV}(\mathbf{r}, t) = K_{IV} \mathcal{U}_{L+L_1} e^{2ik_L Q(\mathbf{r}, t - t_c/2 - t_1)} \times \mathcal{U}_{L+L_1} E_+(L, \mathbf{r}, t - t_c - 2t_1), \quad (\text{A4d})$$

with

$$K_i = \sqrt{T_1} \tau_+, \quad (\text{A5a})$$

$$K_{II} = r_2 r_1 \tau_+ \tau_-, \quad (\text{A5b})$$

$$K_{III} = r_2 \rho_+, \quad (\text{A5c})$$

$$K_{IV} = r_1^2 r_2 \tau_+ \tau_- \varrho_-. \quad (\text{A5d})$$

The operator $\mathcal{U}_d = \exp[i(d/2k_L)\nabla_{\perp}^2]$ accounts for diffraction in the paraxial approximation, corresponding to a propagation distance equal to d . Here $L_1 = z_0$ and $L_2 = L - z_0$, $t_{1,2} = L_{1,2}/c$, and $t_c = 2(t_1 + t_2) = 2L/c$ is the cavity round-trip time. The factors $e^{\pm 2ik_L Q(\mathbf{r}, t)}$ model the phase front modification produced by the reflection on the membrane in the paraxial approximation.

Before continuing, it proves useful to express the coefficients K_{II} , K_{III} , and K_{IV} in terms of the modulus and argument of K_{II} . Let us then write

$$K_{II} = r \exp(i\theta), \quad (\text{A6a})$$

$$K_{III} = K_+ r \exp(i\theta), \quad (\text{A6b})$$

$$K_{IV} = K_- r \exp(i\theta), \quad (\text{A6c})$$

with

$$r = |r_1 r_2 \tau_+ \tau_-|, \quad (\text{A7a})$$

$$\theta = \arg(r_1) + \arg(r_2) + \arg(\tau_+) + \arg(\tau_-), \quad (\text{A7b})$$

$$K_+ = \frac{\varrho_+}{r_1 \tau_+ \tau_-}, \quad (\text{A7c})$$

$$K_- = r_1 \varrho_-. \quad (\text{A7d})$$

Remembering that the mirrors' transmittances are small, so we assume, in particular, $T_j = O(\varrho)$, we have $r = |r_1 r_2| \tau^2 = |r_1 r_2| + O(\varrho^2)$. Expressing $|r_j| = \sqrt{1 - T_j}$, we get then

$$r = 1 - \frac{1}{2}(T_1 + T_2) + O(\varrho^2). \quad (\text{A8})$$

Further, taking into account that $\arg(K_+) + \arg(K_-) = \pi$ [see (A7c), (A7d), and (A1)], we note that

$$K_{\pm} = \mp \varrho \exp(\mp i\beta) + O(\varrho^2), \quad (\text{A9})$$

where we have defined $\beta = \arg(r_1) + \arg(\varrho_-)$.

We denote the slowly varying complex amplitude of $E_+(L, \mathbf{r}, t)$ by $A(\mathbf{r}, t)$, so that $E_+(L, \mathbf{r}, t) = i\mathcal{V}A(\mathbf{r}, t)e^{ik_L L - i\omega_L t}$, where $\mathcal{V} = \sqrt{\hbar\omega_c/4\varepsilon_0 L}$ is a suitable factor with dimensions of voltage, chosen in such a way that $|A(\mathbf{r}, t)|^2$ can be interpreted as the number of photons per unit area which arrive at point \mathbf{r} of the mirror during a round trip, which is convenient to make contact with quantum theory; see the next section. When the expressions (A4) of the partial waves are introduced into (A3) and all the fields are expressed in terms of the complex amplitude A , we get, shifting time for convenience as $t \rightarrow t + t_c$,

$$\begin{aligned} & A(\mathbf{r}, t + t_c) - A(\mathbf{r}, t) \\ &= \sqrt{T_1} \tau_- \mathcal{U}_L A_{\text{inj}}(0, \mathbf{r}, t + t_c/2) + (r e^{i\psi} \mathcal{U}_{2L} - 1) A(\mathbf{r}, t) \\ &\quad - \varrho e^{i\psi} r \mathcal{U}_{L_2} e^{-2ik_L[\bar{z}_0 + Q(\mathbf{r}, t + t_c - t_2)]} \mathcal{U}_{L_2} A(\mathbf{r}, t + 2t_1) \\ &\quad + \varrho e^{i\psi} r \mathcal{U}_{L+L_1} e^{2ik_L[\bar{z}_0 + Q(\mathbf{r}, t + t_c + t_2)]} \mathcal{U}_{L+L_1} A(\mathbf{r}, t - 2t_1), \end{aligned} \quad (\text{A10})$$

where we have subtracted $A(\mathbf{r}, t)$ from both sides for convenience, and we have defined

$$\Psi = 2k_L L + \theta, \quad (\text{A11a})$$

$$\tilde{z}_0 = z_0 + \beta/2k_L. \quad (\text{A11b})$$

Note that the left-hand side of Eq. (A10) can be approximated by $t_c \partial_t A(\mathbf{r}, t)$, whenever its right-hand side is small; it can be approximated more rigorously, when the right-hand side is written as $\mathcal{L}A(\mathbf{r}, t)$, the approximation holds whenever \mathcal{L} is a small operator. Inspection of the equation shows that this is satisfied provided that $\varrho \ll 1$, as already assumed, and $e^{i\Psi} r \mathcal{U}_{2L} - 1 = O(\varrho)$. This second condition requires that (i) $\Psi = 2m\pi + \delta$, with $m \in \mathbb{Z}$ and δ an $O(\varrho)$ normalized detuning whose value is controlled by the injection frequency [see Eq. (A11a)], and (ii) \mathcal{U}_{2L} can be approximated as $1 + i(L/k_L)\nabla_{\perp}^2$, with the effect of the last term on the order of ϱ , which is affected by the choice of a sufficiently small value of L (small diffraction, see Sec. 2 of this Appendix below). Under these conditions, $e^{i\Psi}$, r , \mathcal{U}_{L_2} , and \mathcal{U}_{L+L_1} in the last two terms can be approximated by 1 (note that these terms already contain ϱ as a factor), while $A(\mathbf{r}, t \pm 2t_1)$ can be set to $A(\mathbf{r}, t)$, since $A(\mathbf{r}, t \pm 2t_1) \simeq A(\mathbf{r}, t) \pm 2t_1 \partial_t A(\mathbf{r}, t)$, but $2t_1 \partial_t A(\mathbf{r}, t) \sim t_c \partial_t A(\mathbf{r}, t) = O(\varrho)$. There remains to make a last simplification, consisting of approximating $Q(\mathbf{r}, t + t_c \pm t_2)$ by $Q(\mathbf{r}, t)$ in the exponentials. Note that $Q(\mathbf{r}, t + t_c \pm t_2) \approx Q(\mathbf{r}, t) + (t_c \pm t_2) \partial_t Q(\mathbf{r}, t)$, and we have checked self-consistently that the last term is on the order of ϱ or smaller in our simulations. This last approximation leads us then to

$$\begin{aligned} \partial_t A(\mathbf{r}, t) &= \frac{1}{t_c} A_0(\mathbf{r}, t) - \frac{T}{2t_c} A + i \left(\frac{\delta}{t_c} + \frac{L}{k_L t_c} \nabla_{\perp}^2 \right) A \\ &+ i \frac{2\varrho}{t_c} \sin[2k_L(\tilde{z}_0 + Q)] A, \end{aligned} \quad (\text{A12})$$

where $A_0(\mathbf{r}, t) = \tau_- \sqrt{T_1} \mathcal{U}_L A_{\text{inj}}(\mathbf{0}, \mathbf{r}, t + t_c/2)$ is the injected field at the plane of the right mirror. Note that $A_0(\mathbf{r}, t) \approx \sqrt{T_1} e^{i \arg(\tau_-)} A_{\text{inj}}(\mathbf{0}, \mathbf{r}, t + t_c/2)$, which basically coincides with the injected field amplitude.

2. Controlling the diffraction

A key point in the previous derivation is the assumption of small diffraction. A very efficient way to deal with this problem is the use of quasi-self-imaging cavities [25], which by means of lenses or other mirrors image both end mirrors very close to each other, leading to an effective ‘‘diffractive length’’ for the cavity, L_{diff} , which can be as small as desired (it can even take negative values). When using such kind of cavities the diffraction operator \mathcal{U}_{2L} , which is the one leading to the diffraction term $iL\nabla_{\perp}^2 A/k_L t_c$ in Eq. (A12), must be replaced with $\mathcal{U}_{2L_{\text{diff}}}$ or, equivalently, the diffraction term in Eq. (A12) must be replaced by $iL_{\text{diff}}\nabla_{\perp}^2 A/k_L t_c$. This way we arrive at the final form of the model,

$$\begin{aligned} \partial_t A(\mathbf{r}, t) &= \frac{1}{t_c} A_0(\mathbf{r}, t) - \frac{T}{2t_c} A + i \left(\frac{\delta}{t_c} + \frac{L_{\text{diff}}}{k_L t_c} \nabla_{\perp}^2 \right) A \\ &+ i \frac{2\varrho}{t_c} \sin[2k_L(\tilde{z}_0 + Q)] A, \end{aligned} \quad (\text{A13})$$

which coincides with Eq. (3) once we introduce the parameters defined there, and the normalized detuning Δ appearing therein is identified with $2\delta/T$. In addition, note that in the main text we have chosen $\beta = -\pi/2$ and $\arg(\tau_-) = 0$ to simplify the notation and connect with previous works.

APPENDIX B: DERIVATION OF THE COUPLING IN THE MECHANICAL EQUATION

In this section we derive the optomechanical coupling term appearing on the right-hand side of the mechanical equation of motion, Eq. (4). We show in the following that this is easily done from the coupling term derived for the optical field in the previous section, together with a (momentary) quantum description of the system. In such description, the fields A and Q are replaced with two operators \hat{A} and \hat{Q} , obeying standard equal-time commutation relations $[\hat{A}(\mathbf{r}, t), \hat{A}^\dagger(\mathbf{r}', t)] = \delta^2(\mathbf{r} - \mathbf{r}')$ [24] and $[\hat{Q}(\mathbf{r}, t), \hat{P}(\mathbf{r}', t)] = i\hbar\delta^2(\mathbf{r} - \mathbf{r}')$, with $\hat{P} = \sigma \partial_t \hat{Q}$ the momentum density field of the membrane (σ is its mass surface density). The coupling between the optical and mechanical fields is described in the quantum theory through an interaction Hamiltonian \hat{H}_{int} , which contributes to the equation of motion of any operator \hat{O} according to Heisenberg’s equation

$$\partial_t \hat{O}|_{\text{int}} = \frac{i}{\hbar} [\hat{H}_{\text{int}}, \hat{O}]. \quad (\text{B1})$$

Now, from the optical equation that we derived in the previous section, we know that when Eq. (B1) is applied to the field $\hat{A}(\mathbf{r}, t)$, we should get

$$\partial_t \hat{A}(\mathbf{r}, t)|_{\text{int}} = i \frac{2\varrho}{t_c} \sin\{2k_L[\tilde{z}_0 + \hat{Q}(\mathbf{r}, t)]\} \hat{A}, \quad (\text{B2})$$

and hence the interaction Hamiltonian must have the form

$$\begin{aligned} \hat{H}_{\text{int}} &= -\hbar \int d^2\mathbf{r} \frac{2\varrho}{t_c} \sin\{2k_L[\tilde{z}_0 + \hat{Q}(\mathbf{r}, t)]\} \\ &\times \hat{A}^\dagger(\mathbf{r}, t) \hat{A}(\mathbf{r}, t). \end{aligned} \quad (\text{B3})$$

On the other hand, once we know the interaction Hamiltonian, we can particularize the Heisenberg equation (B1) to the mechanical momentum density field, obtaining

$$\partial_t \hat{P}(\mathbf{r}, t)|_{\text{int}} = \frac{4k_L\varrho}{t_c} \cos\{2k_L[\tilde{z}_0 + \hat{Q}(\mathbf{r}, t)]\} \hat{A}^\dagger(\mathbf{r}, t) \hat{A}(\mathbf{r}, t), \quad (\text{B4})$$

where we have used the property

$$[F(\hat{Q}(\mathbf{r}', t)), \hat{P}(\mathbf{r}, t)] = i\hbar(\partial F/\partial \hat{Q})\delta^2(\mathbf{r} - \mathbf{r}'), \quad (\text{B5})$$

valid for any function F ; the classical limit of this expression, $\{\hat{Q}, \hat{P}, \hat{A}, \hat{A}^\dagger\} \rightarrow \{Q, \sigma \partial_t Q, A, A^*\}$, provides the coupling appearing in Eq. (4),

$$\partial_t^2 Q(\mathbf{r}, t)|_{\text{int}} = \frac{4\hbar k_L \rho}{\sigma t_c} \cos\{2k_L[\tilde{z}_0 + Q(\mathbf{r}, t)]\} |A(\mathbf{r}, t)|^2, \quad (\text{B6})$$

where note that in the main text we have taken $\beta = -\pi/2$ and hence $2k_L \tilde{z}_0 = 2k_L z_0 - \pi/2$ for simplicity and definiteness.

APPENDIX C: LINEAR AND QUADRATIC MODELS AND THEIR NORMALIZATION

Starting from the general model equations (3) and (4), in this section we provide a detailed derivation of the quadratic and linear models introduced in Eqs. (5). Consider the interaction terms of Eqs. (3) and (4), which can be written as

$$\partial_t A|_{\text{int}} = -i \frac{4\gamma_c \varrho}{T} \cos[2k_L(z_0 + Q)]A, \quad (\text{C1a})$$

$$\partial_t^2 Q|_{\text{int}} = \frac{4\varrho \hbar k_L}{\sigma t_c} \sin[2k_L(z_0 + Q)]|A|^2. \quad (\text{C1b})$$

Taking into account that the mechanical displacement is typically much smaller than the optical wavelength, we can expand the trigonometric functions around $Q = 0$, obtaining

$$\begin{aligned} \cos[2k_L(z_0 + Q)] &\approx \cos(2k_L z_0)(1 - k_L^2 Q^2) \\ &\quad - 2k_L \sin(2k_L z_0)Q, \end{aligned} \quad (\text{C2a})$$

$$\begin{aligned} \sin[2k_L(z_0 + Q)] &\approx \sin(2k_L z_0)(1 - k_L^2 Q^2) \\ &\quad + 2k_L \cos(2k_L z_0)Q. \end{aligned} \quad (\text{C2b})$$

The interaction terms admit then different approximations depending on where the membrane is located. In particular, when $\cos(2k_L z_0) = \pm 1$ and $\sin(2k_L z_0) = 0$, that is, $z_0/\lambda_L = n/4$, with $n = 0, 1, 2, \dots$, the sign of the cosine being positive (negative) for even (odd) n , we get

$$\partial_t A|_{\text{int}} \approx \pm i \frac{4\gamma_c \varrho}{T} (k_L^2 Q^2 - 1)A, \quad (\text{C3a})$$

$$\partial_t^2 Q|_{\text{int}} \approx \pm \frac{8\varrho \hbar k_L^2}{\sigma t_c} Q|A|^2, \quad (\text{C3b})$$

leading to the model equations

$$\partial_t A = \gamma_c \mathcal{E} + \gamma_c(-1 + i\Delta_{\pm} + i l_c^2 \nabla_{\perp}^2)A \pm i \frac{4\gamma_c k_L^2 \varrho}{T} Q^2 A, \quad (\text{C4a})$$

$$\partial_t^2 Q + \gamma_m \partial_t Q + (\Omega_m^2 - v_m^2 \nabla_{\perp}^2)Q = \pm \frac{8\varrho \hbar k_L^2}{\sigma t_c} Q|A|^2, \quad (\text{C4b})$$

where $\Delta_{\pm} = \Delta \mp 4\varrho/T$ is a shifted detuning. It is convenient both for the numerical and the analytical analysis to introduce the normalized time $\tau = \gamma_c t$ and spatial coordinates $\bar{\mathbf{r}} = \mathbf{r}/l_c$, plus variables and parameters

$$\begin{aligned} Z &= \sqrt{\frac{8\varrho}{T}} k_L Q, & F &= \sqrt{\frac{8\varrho \hbar k_L^2}{\sigma t_c \Omega_m^2}} A, \\ E &= \sqrt{\frac{8\varrho \hbar k_L^2}{\sigma t_c \Omega_m^2}} \mathcal{E}, \end{aligned} \quad (\text{C5})$$

and

$$\gamma = \frac{\gamma_m}{\gamma_c}, \quad \Omega = \frac{\Omega_m}{\gamma_c}, \quad (\text{C6})$$

which transform the previous equations into

$$\partial_{\tau} F = [-1 + i(\Delta + \nabla^2 \pm Z^2)]F + E, \quad (\text{C7a})$$

$$\partial_{\tau}^2 Z + \gamma \partial_{\tau} Z + \Omega^2(1 - \rho^2 \nabla^2)Z = \pm \Omega^2 Z|F|^2, \quad (\text{C7b})$$

where $\nabla^2 = l_c^2(\partial_x^2 + \partial_y^2) = (\partial_{\bar{x}}^2 + \partial_{\bar{y}}^2)$ and $\rho = v_m/\Omega_m l_c$ is the ‘‘effective rigidity parameter’’ discussed in the main text. In the case of the positive sign, this is the equation that we introduced in the main text defining the quadratic model, Eqs. (5) with $\mu = 2$. The negative sign case is not interesting because no pattern forming instabilities are found, and hence we have not introduced it in the main text.

Let us consider now the case $\cos(2k_L z_0) = 0$ and $\sin(2k_L z_0) = \pm 1$, that is, $z_0/\lambda_L = (2n + 1)/8$ with $n = 0, 1, 2, \dots$, the sign of the sine function being positive (negative) for even (odd) n . This choice leads to

$$\partial_t A|_{\text{int}} \approx \pm i \frac{8\gamma_c k_L \varrho}{T} Q A, \quad (\text{C8a})$$

$$\partial_t^2 Q|_{\text{int}} \approx \pm \frac{4\varrho \hbar k_L}{\sigma t_c} |A|^2, \quad (\text{C8b})$$

and hence to the model equations

$$\partial_t A = \gamma_c \mathcal{E} + \gamma_c(-1 + i\Delta + i l_c^2 \nabla_{\perp}^2)A \pm i \frac{8\gamma_c k_L \varrho}{T} Q A, \quad (\text{C9a})$$

$$\partial_t^2 Q + \gamma_m \partial_t Q + (\Omega_m^2 - v_m^2 \nabla_{\perp}^2)Q = \pm \frac{4\varrho \hbar k_L}{\sigma t_c} |A|^2. \quad (\text{C9b})$$

In this case, the most convenient normalization is the same as before, except for the fields and pump parameter, which are normalized as

$$\begin{aligned} Z &= \pm \frac{8k_L \varrho}{T} Q, & F &= \sqrt{\frac{32\varrho^2 \hbar k_L^2}{\sigma t_c \Omega_m^2}} A, \\ E &= \sqrt{\frac{32\varrho^2 \hbar k_L^2}{\sigma t_c \Omega_m^2}} \mathcal{E}. \end{aligned} \quad (\text{C10})$$

These normalizations transform the previous equations into

$$\partial_{\tau} F = [-1 + i(\Delta + \nabla^2 + Z)]F + E, \quad (\text{C11a})$$

$$\partial_{\tau}^2 Z + \gamma \partial_{\tau} Z + \Omega^2(1 - \rho^2 \nabla^2)Z = \Omega^2 |F|^2, \quad (\text{C11b})$$

precisely the equation that we introduced in the main text defining the linear model, Eqs. (5), with $\mu = 1$.

APPENDIX D: DETAILS OF THE LINEAR STABILITY ANALYSIS

In the following we explain how we have performed the stability analysis of the homogeneous, stationary solutions associated with the model equations (5), which we gave in the main text. We have followed the standard linear stability analysis, by studying the evolution of small perturbations $(\delta F, \delta Z)$ added to the steady solution (\bar{F}, \bar{Z}) . Upon linearizing the model equations (5) with respect to $(\delta F, \delta Z)$, expressing them in terms of the normal mode basis of the uncoupled mechanical and optical systems (plane waves) as $\delta F(\bar{\mathbf{r}}, \tau) = \sum_{\mathbf{k}} \phi_{\mathbf{k}}(\tau) e^{i\mathbf{k}\cdot\bar{\mathbf{r}}}$ and $\delta Z(\bar{\mathbf{r}}, \tau) = \sum_{\mathbf{k}} \zeta_{\mathbf{k}}(\tau) e^{i\mathbf{k}\cdot\bar{\mathbf{r}}}$ (note that $\zeta_{-\mathbf{k}}^* = \zeta_{\mathbf{k}}$ because δZ is a real field), and equating coefficients of like exponentials, we get, for each \mathbf{k} , a linear system of differential equations for the modal perturbations $\mathbf{v} \equiv (\phi_{\mathbf{k}}, \phi_{-\mathbf{k}}^*, \zeta_{\mathbf{k}})$. Owing to this linearity and the time invariance of the system, its solutions have the

form $\mathbf{v}(\tau) = \mathbf{v}(0)e^{\lambda\tau}$. Upon making such substitution, a homogeneous linear system of algebraic equations in $\mathbf{v}(0)$ is attained, whose condition for existence of nontrivial solutions can be written as $C(k^2; \lambda) \equiv \sum_{n=0}^4 c_n(k^2)\lambda^n = 0$, where $k = |\mathbf{k}|$.

In the case of the linear model and after simple algebra, we get

$$c_4 = 1, \quad c_3 = 2 + \gamma, \quad (\text{C12a})$$

$$c_2 = 1 + 2\gamma + \Omega_k^2 + \Delta_k^2, \quad (\text{C12b})$$

$$c_1 = \gamma(1 + \Delta_k^2) + 2\Omega_k^2, \quad (\text{C12c})$$

$$c_0 = 2\bar{Z}_{\text{LM}}\Delta_k\Omega_k^2 + (1 + \Delta_k^2)\Omega_k^2, \quad (\text{C12d})$$

where $\Omega_k^2 \equiv \Omega^2(1 + \rho^2k^2)$ and $\Delta_k \equiv \Delta - k^2 + \bar{Z}_{\text{LM}}$. On the other hand, the quadratic model leads to

$$c_4 = c_3 = 0, \quad c_2 = 1, \quad c_1 = \gamma, \quad (\text{C13a})$$

$$c_0 = \Omega^2[1 + \rho^2k^2 - E^2/(1 + \Delta^2)], \quad (\text{C13b})$$

for the trivial solution ($\bar{Z}_{\text{QM}} = 0$) and

$$c_4 = 1, \quad c_3 = 2 + \gamma, \quad (\text{C14a})$$

$$c_2 = 1 + 2\gamma + \mu_k^2 + \Omega^2\rho^2k^2, \quad (\text{C14b})$$

$$c_1 = \gamma(1 + \mu_k^2) + 2\Omega^2\rho^2k^2, \quad (\text{C14c})$$

$$c_0 = [\rho^2k^2(1 + \mu_k^2) + 4\mu_k(\bar{Z}_{\text{QM}}^2 - \Delta)]\Omega^2, \quad (\text{C14d})$$

for the nontrivial solution $\bar{Z}_{\text{QM}}^2 = \sqrt{E^2 - 1}$, with $\mu_k = \bar{Z}_{\text{QM}}^2 - k^2$.

We observe that the growth exponents $\lambda(k^2)$, solutions to $C(k^2; \lambda) = 0$, depend on k and not on \mathbf{k} because of the rotational invariance of both the steady state and the model equations. Whenever $\text{Re}\{\lambda\} < 0$ for all k the steady state is stable, while if $\text{Re}\{\lambda\} > 0$ for some k it is unstable. The condition $\text{Re}\{\lambda\} = 0$ thus defines a possible instability, or bifurcation, which is met either when $\lambda = 0$ (static, or pitchfork bifurcation: $c_0 = 0$) or when $\lambda = i\sqrt{c_1/c_3}$ (self-pulsing or Hopf bifurcation: $c_1c_2c_3 = c_4c_1^2 + c_3^2c_0$). On the other hand, when the bifurcation is associated with $k = 0$ the new state is spatially uniform (homogeneous instability),

while if $k \neq 0$ the instability is pattern forming. In both the linear and the quadratic models the expressions for the $c_n(k^2)$ coefficients are simple enough as to allow us to locate all the static instabilities analytically, while the Hopf instabilities can be efficiently and systematically found numerically, and even analytically in the experimentally relevant limits $\gamma \ll 1$ and $\Omega \gg 1$. We will give further details in future works.

APPENDIX E: DETAILS OF THE NUMERICAL SIMULATION OF THE MODEL EQUATIONS

As explained in the main text, we have performed an extensive numerical analysis of the patterns appearing in the model equations (5), and here we want to say a few words about the method we have used, as well as show some examples of the transverse structures which we have found.

We have performed the numerical simulation of the evolution equations by using a symmetrized split-step Fourier method, whose name comes from the fact that it treats the linear and nonlinear terms of the evolution equations separately, alternating them in short time steps. The linear evolution is computed in the spatial frequency domain by using the fast Fourier transform; as for the evolution coming from the nonlinear terms, it turns out that we can solve it exactly at every step for these model equations. The method is exact up to second order in the (normalized) time step, and, given that we move to the Fourier domain in the spatial variables, it naturally requires periodic boundary conditions in the chosen spatial window (although fixed boundary conditions can be simulated as well, simply by forcing the fields to have the desired values, typically zero, at the boundaries, as we do in Sec. IV). We have carried simulations of the model equations in both 1D and 2D, finding periodic patterns (which turn out to be hexagons in 2D) and localized structures which satisfy all the properties of cavity solitons (e.g., they can be written and erased individually). From a numerical point of view, in order to find periodic patterns, the reciprocal spatial lattice which we choose has to contain the wave vectors which form such pattern. In the case of the localized structures, the spatial window has to be large enough to hold the number of solitons which we want to write, as well as allow for their mobility if that is the case.

-
- [1] J. M. Raimond, M. Brune, and S. Haroche, *Rev. Mod. Phys.* **73**, 565 (2001); H. Walther, B. T. H. Varcoe, B.-G. Englert, and Th. Becker, *Rep. Prog. Phys.* **69**, 1325 (2006).
- [2] D. Jaksch and P. Zoller, *Ann. Phys.* **315**, 52 (2004); M. Lewenstein, A. Sanpera, and V. Ahufinger, *Ultracold Atoms In Optical Lattices: Simulating Quantum Many-body Systems* (Oxford University Press, New York, 2012).
- [3] D. Leibfried, R. Blatt, C. Monroe, and D. Wineland, *Rev. Mod. Phys.* **75**, 281 (2003); Ch. Schneider, D. Porras, and T. Schaetz, *Rep. Prog. Phys.* **75**, 024401 (2012).
- [4] M. H. Devoret, A. Wallraff, and J. M. Martinis, [arXiv:cond-mat/0411174](https://arxiv.org/abs/cond-mat/0411174); J. Q. You and F. Nori, *Phys. Today* **58**, 42 (2005).
- [5] B. Urbaszek, X. Marie, T. Amand, O. Krebs, P. Voisin, P. Maletinsky, A. Hoge, and A. Imamoglu, *Rev. Mod. Phys.* **85**, 79 (2013).
- [6] K. Hammerer, A. S. Sørensen, and E. S. Polzik, *Rev. Mod. Phys.* **82**, 1041 (2010); C. A. Muschik, H. Krauter, K. Hammerer, and E. S. Polzik, *Quantum Inf. Process.* **10**, 839 (2011).
- [7] T. J. Kippenberg and K. J. Vahala, *Opt. Express* **15**, 17172 (2007); F. Marquardt and S. M. Girvin, *Physics* **2**, 40 (2009); M. Aspelmeyer, T. J. Kippenberg, and F. Marquardt, *Rev. Mod. Phys.* **86**, 1391 (2014).
- [8] A. Dorsel, J. D. McCullen, P. Meystre, E. Vignes, and H. Walther, *Phys. Rev. Lett.* **51**, 1550 (1983); P. Meystre, E. M. Wright, J. D. McCullen, and E. Vignes, *J. Opt. Soc. Am. B* **2**, 1830 (1985).
- [9] L. A. Lugiato and R. Lefever, *Phys. Rev. Lett.* **58**, 2209 (1987).
- [10] T. J. Kippenberg, H. Rokhsari, T. Carmon, A. Scherer, and K. J. Vahala, *Phys. Rev. Lett.* **95**, 033901 (2005); O. Arcizet,

- P.-F. Cohadon, T. Briant, M. Pinard, and A. Heidmann, *Nature (London)* **444**, 71 (2006); A. Schliesser, P. Del'Haye, N. Nooshi, K. J. Vahala, and T. J. Kippenberg, *Phys. Rev. Lett.* **97**, 243905 (2006).
- [11] S. Weis, R. Rivière, S. Deléglise, E. Gavartin, O. Arcizet, A. Schliesser, and T. J. Kippenberg, *Science* **330**, 1520 (2010); J. D. Teufel, D. Li, M. S. Allman, K. Cicak, A. J. Sirois, J. D. Whittaker, and R. W. Simmonds, *Nature (London)* **471**, 204 (2011); A. H. Safavi-Naeini, T. P. Mayer Alegre, J. Chan, M. Eichenfield, M. Winger, Q. Lin, J. T. Hill, D. E. Chang, and O. Painter, *ibid.* **472**, 69 (2011).
- [12] C. Fabre, M. Pinard, S. Bourzeix, A. Heidmann, E. Giacobino, and S. Reynaud, *Phys. Rev. A* **49**, 1337 (1994).
- [13] S. Mancini and P. Tombesi, *Phys. Rev. A* **49**, 4055 (1994).
- [14] D. W. C. Brooks, T. Botter, S. Schreppler, T. P. Purdy, N. Brahms, and D. M. Stamper-Kurn, *Nature (London)* **488**, 476 (2012).
- [15] A. H. Safavi-Naeini, S. Gröblacher, J. T. Hill, J. Chan, M. Aspelmeyer, and O. Painter, *Nature (London)* **500**, 185 (2013).
- [16] G. Heinrich, M. Ludwig, J. Qian, B. Kubala, and F. Marquardt, *Phys. Rev. Lett.* **107**, 043603 (2011).
- [17] F. Marino and F. Marin, *Phys. Rev. E* **83**, 015202(R) (2011).
- [18] A. Butsch, C. Conti, F. Biancalana, and P. St. J. Russell, *Phys. Rev. Lett.* **108**, 093903 (2012); C. Conti, A. Butsch, F. Biancalana, and P. St. J. Russell, *Phys. Rev. A* **86**, 013830 (2012).
- [19] E. Tesio, G. R. M. Robb, T. Ackemann, W. J. Firth, and G.-L. Oppo, *Phys. Rev. A* **86**, 031801(R) (2012); *Opt. Express* **21**, 26144 (2013); G. Labeyrie, E. Tesio, P. M. Gomes, G.-L. Oppo, W. J. Firth, G. R. M. Robb, A. S. Arnold, R. Kaiser, and T. Ackemann, *Nat. Photon.* **8**, 321 (2014).
- [20] R. Horodecki, P. Horodecki, M. Horodecki, and Karol Horodecki, *Rev. Mod. Phys.* **81**, 865 (2009).
- [21] O. Pfister, S. Feng, G. Jennings, R. Pooser, and D. Xie, *Phys. Rev. A* **70**, 020302(R) (2004); N. C. Menicucci, S. T. Flammia, H. Zaidi, and O. Pfister, *ibid.* **76**, 010302(R) (2007); M. Pysker, Y. Miwa, R. Shahrokhshahi, R. Bloomer, and O. Pfister, *Phys. Rev. Lett.* **107**, 030505 (2011); R. Shahrokhshahi and O. Pfister, *Quantum Inf. Comput.* **12**, 0953 (2012).
- [22] G. Patera, C. Navarrete-Benlloch, G. J. de Valcárcel, and C. Fabre, *Eur. Phys. J. D* **66**, 241 (2012).
- [23] K. Staliunas and V. J. Sánchez-Morcillo, *Transverse Patterns in Nonlinear Optical Resonators* (Springer, Berlin, 2003).
- [24] L. A. Lugiato and G. Grynberg, *Europhys. Lett.* **29**, 675 (1995); L. A. Lugiato and A. Gatti, *Phys. Rev. Lett.* **70**, 3868 (1993); A. Gatti and L. A. Lugiato, *Phys. Rev. A* **52**, 1675 (1995); I. Pérez-Arjona, E. Roldán, and G. J. de Valcárcel, *Europhys. Lett.* **74**, 247 (2006); *Phys. Rev. A* **75**, 063802 (2007).
- [25] J. A. Arnaud, *Appl. Opt.* **8**, 189 (1969).
- [26] S. Kolpakov, A. Esteban-Martín, F. Silva, J. García, K. Staliunas, and G. J. de Valcárcel, *Phys. Rev. Lett.* **101**, 254101 (2008).
- [27] V. B. Taranenko, K. Staliunas, and C. O. Weiss, *Phys. Rev. Lett.* **81**, 2236 (1998); A. Esteban-Martín, J. García, E. Roldán, V. B. Taranenko, G. J. de Valcárcel, and C. O. Weiss, *Phys. Rev. A* **69**, 033816 (2004).
- [28] B. Chalopin, A. Chiummo, C. Fabre, A. Maître, and N. Treps, *Opt. Express* **18**, 8033 (2010).
- [29] B. Chalopin, F. Scazza, C. Fabre, and N. Treps, *Opt. Express* **19**, 4405 (2011).
- [30] J. Liu, F. A. Torres, Y. Ma, C. Zhao, L. Ju, D. G. Blair, S. Chao, I. Roch-Jeune, R. Flaminio, C. Michel, and K.-Y. Liu, *Appl. Opt.* **53**, 841 (2014).
- [31] M. C. Cross and P. C. Hohenberg, *Rev. Mod. Phys.* **65**, 851 (1993).
- [32] J. D. Thompson, B. M. Zwickl, A. M. Jayich, F. Marquardt, S. M. Girvin, and J. G. E. Harris, *Nature (London)* **452**, 72 (2008).
- [33] A. M. Jayich, J. C. Sankey, B. M. Zwickl, C. Yang, J. D. Thompson, S. M. Girvin, A. A. Clerk, F. Marquardt, and J. G. E. Harris, *New J. Phys.* **10**, 095008 (2008).
- [34] W. J. Firth and C. O. Weiss, *Opt. Photon. News* **13**, 54 (2002).
- [35] B. M. Zwickl, W. E. Shanks, A. M. Jayich, C. Yang, A. C. Bleszynski Jayich, J. D. Thompson, and J. G. E. Harris, *Appl. Phys. Lett.* **92**, 103125 (2008).
- [36] J. C. Sankey, C. Yang, B. M. Zwickl, A. M. Jayich, and J. G. E. Harris, *Nat. Phys.* **6**, 707 (2010).
- [37] D. J. Wilson, C. A. Regal, S. B. Papp, and H. J. Kimble, *Phys. Rev. Lett.* **103**, 207204 (2009).
- [38] M. Karuza, C. Molinelli, M. Galassi, C. Biancofiore, R. Natali, P. Tombesi, G. Di Giuseppe, and D. Vitali, *New J. Phys.* **14**, 095015 (2012).
- [39] M. Karuza, M. Galassi, C. Biancofiore, C. Molinelli, R. Natali, P. Tombesi, G. Di Giuseppe, and D. Vitali, *J. Opt.* **15**, 025704 (2013).
- [40] M. Karuza, C. Biancofiore, M. Bawaj, C. Molinelli, M. Galassi, R. Natali, P. Tombesi, G. Di Giuseppe, and D. Vitali, *Phys. Rev. A* **88**, 013804 (2013).
- [41] U. Kemiktarak, M. Metcalfe, M. Durand, and J. Lawall, *Appl. Phys. Lett.* **100**, 061124 (2012).
- [42] U. Kemiktarak, M. Durand, M. Metcalfe, and J. Lawall, *New J. Phys.* **14**, 125010 (2012).
- [43] U. Kemiktarak, M. Durand, C. Stambaugh, and J. Lawall, *Proc. SPIE* **8633**, 8633N-1 (2013).
- [44] C. Navarrete-Benlloch, E. Roldán, and G. J. de Valcárcel, *Phys. Rev. Lett.* **100**, 203601 (2008); C. Navarrete-Benlloch, G. J. de Valcárcel, and E. Roldán, *Phys. Rev. A* **79**, 043820 (2009); C. Navarrete-Benlloch, A. Romanelli, E. Roldán, and G. J. de Valcárcel, *ibid.* **81**, 043829 (2010); C. Navarrete-Benlloch, Contributions to the quantum optics of multi-mode optical parametric oscillators, Ph.D. thesis, Universitat de València, 2011, [arXiv:1504.05917](https://arxiv.org/abs/1504.05917).
- [45] A. Luis and L. L. Sánchez-Soto, *Quantum Semiclass. Opt.* **7**, 153 (1995).